Pergamon

NanoStructured Materials, Vol. 7, Nos. 1/2, pp. 137–146, 1996
Elsevier Science Ltd

0965-9773/96 $15.00 + .00

SSDI 0965-9773(95)00303-7

MORPHOLOGY AND CRYSTALLOGRAPHY OF NANO-PARTICULATES REVEALED BY ELECTRON HOLOGRAPHY

L.F. Allard, E. Völkl, A. Carim[a], A.K. Datye[b] and R. Ruoff[c]

Oak Ridge National Laboratory, Oak Ridge, TN 37831-6064, U.S.A.
[a]Penn State University, College Park, PA, U.S.A.
[b]University of New Mexico, Albuquerque, NM, U.S.A.
[c]SRI International, Menlo Park, CA, U.S.A.

(Accepted August 1995)

Abstract *— Electron holography permits the precise determination of aspects of the morphology of nanometer-sized particulates, because the pure phase information in the image wave can be reconstructed and displayed. Profiles of intensity over the phase image are, in particularly advantageous cases, directly related to particle morphology, since the phase intensity for materials that are essentially kinematic scatterers and are of homogeneous composition is directly related to thickness. Holograms at high resolution can also be used for many other analyses of a material's structure; they provide, for example, a method for precise calibration of lattice spacings in nanometer-sized areas, that allows for the correlation of structure to processing parameters. Examples of the use of holography for studies of nanoparticles of oxides and model catalysts are given.*

INTRODUCTION

The properties and behavior of nanostructured materials are dependent not only upon processing parameters, but also upon nanometer-scale and atomic-level characteristics of the precursor particles. Characteristics such as surface morphology (*i.e.* the exact nature of crystallographic facets comprising a particle's surface), internal structures such as voids and crystalline defects, and surface composition can have significant effects, *e.g.*, on the consolidation behavior and final microstructure of sintered nanomaterials or on the behavior of supported metal catalysts. In order to fully understand the important microstructural features which control processing and properties, techniques of electron microscopy are commonly employed.

Conventional and even field-emission scanning electron microscopies provide little information for particles that are under 10 nm in mean diameter (1). In order to observe features such as surface faceting or internal defects, transmission electron microscopy (TEM) or scanning probe techniques are necessary. The full characterization of a particle's three-dimensional structure is, however, still difficult to achieve with conventional applications of these techniques. The newly emerging technique of electron holography can, by separating the phase and amplitude components of a transmitted electron wave, provide relative thickness information with atomic level

sensitivity for each point in the image. This capability relies on the highly coherent electron beam generated by a field emission gun, and provides an experimentally straightforward way of assessing morphology in nanoparticles. In the present paper, the technique of electron holography will be briefly described, and its application to determination of morphologies of nanoparticles such as ZrO_2 used for nanostructured ceramics, and Pd on SiO_2 used as a model combustion catalyst. Its usefulness in giving precise information on crystal lattice spacings in nanocrystals is also shown, with application to studies of giant nested fullerene materials.

EXPERIMENTAL

The principles of electron holography are described in detail elsewhere (*e.g.* (2,3)), and are only reviewed briefly here. Our holograms were acquired digitally using a Hitachi HF-2000 cold FEG-TEM operated at 200 kV. A Möllenstedt biprism (4) positioned between the first and second intermediate lenses was used to form the holograms. The biprism consists simply of a gold-coated drawn quartz fiber 0.3 mm in diameter, which is positioned normal to the electron beam and is rotatable for optimum alignment. A voltage is supplied to the biprism fiber by a Keithley 487 picoammeter/voltage source, which provides up to 500 volts at a stability of 10^{-6} (about 10 times more stable than a battery). The specimen is placed so the image wave passes on one side of the fiber and the coherent plane wave from the illumination system passes on the other side of the fiber. As the voltage is increased, the two waves are bent towards each other and an interference pattern is developed consisting of fine parallel fringes. Because the electron wave undergoes phase changes as it passes through the specimen, the fringes in the interference pattern vary in position and intensity in direct relation to the phase information contained in the image wave. A Fourier transform of the hologram yields a pattern composed of a central power spectrum, or autocorrelation, along with two sidebands whose distance from the pattern center is inversely related to the fringe spacing. Since the phase information is contained in the deflection of the interference fringes within the material, digital reconstruction of the image from either of these sidebands provides a complex image that can be separated into amplitude and phase components.

The biprism voltage was adjusted to give 0.1 nm or finer fringes (referred to the specimen) having contrast greater than 25% at magnifications of 700 kX and 1 MX. Holograms were recorded digitally using a 1k x 1k CCD slow scan camera (Gatan, Inc., Model 694), and phase images were reconstructed and quantitative measurements from the holograms were made using the Holoworks© software package (5), now commercially available from Gatan.

RESULTS

ZrO_2 Nanocrystals

The intensity at any point in the reconstructed phase image from an off-axis electron hologram represents the change in phase of the electron wavefront with respect to the reference wave. This phase change is proportional to the mean inner potential of the material and the local thickness of the material through which the electron beam is passing (6,7). If the sample material is uniform, as is the case for the nanocrystalline ceramic particles discussed here, then the inner potential does not vary over the field of view and any changes in the intensity of the phase image can be directly ascribed to thickness variations.

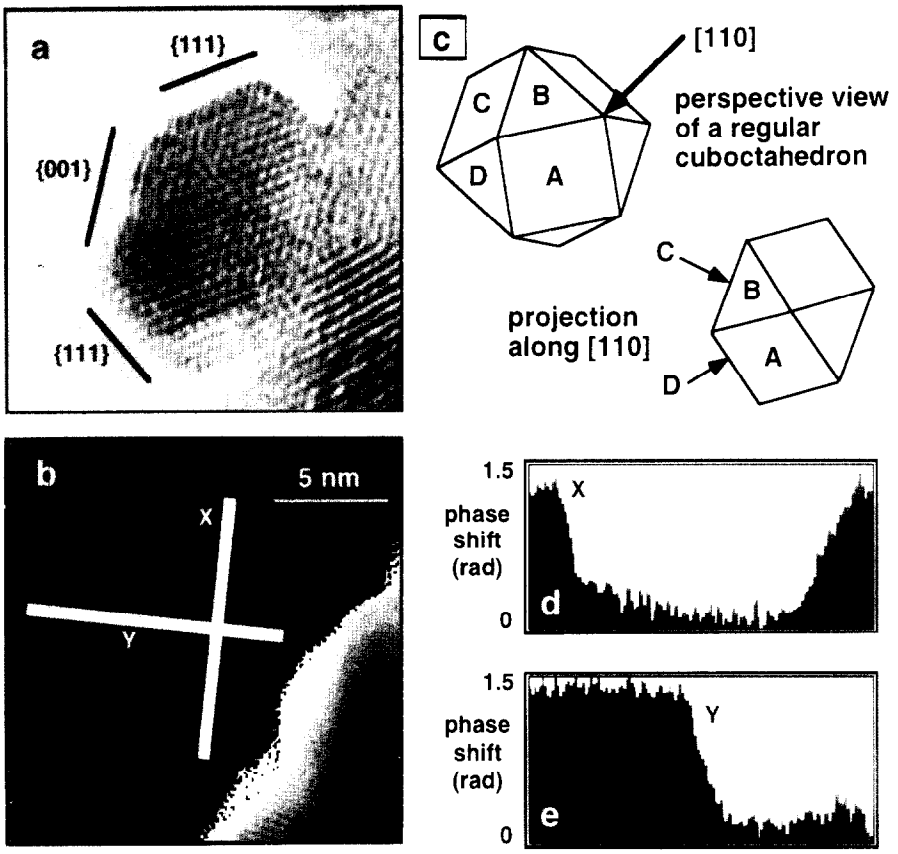

Figure 1. (a) High resolution TEM image of zirconia particle in a <110> zone axis orientation; (b) phase image reconstructed from the hologram of the particle, showing lines X and Y across which phase profiles of (d) and (e) were taken; (c) cuboctahedron in perspective and projected views, showing the outline of the particle expected from a <110> projection. See text for details.

Although nanocrystalline zirconia particles often exhibit faceting and thus appear to be polyhedral from high-resolution images, the actual shapes of such particles have not previously been determined. The apparent bounding planes generally lie along {111} and {001}, so it is natural to assume that the particle shapes are cuboctahedral (or tetrakaidecahedral).

Figure 1(a) shows a nanocrystalline zirconia particle and Figure 1(b) the corresponding phase information. This particle is in a <110> zone axis orientation (as determined from analysis of the high resolution image and corresponding hologram) and it appears to be cuboctahedral based on the bounding planes and overall projected shape. The relative lengths of the facets suggests a polyhedral morphology approximately halfway between an octahedron and a cube. Figure 1(c) shows a sketch of the <110> projection of a cuboctahedron showing the correspondence between the particle and the model. The line profiles through the phase image, however, are not consistent with the anticipated particle shape. If the particle were cuboctahedral, the profile inward from the

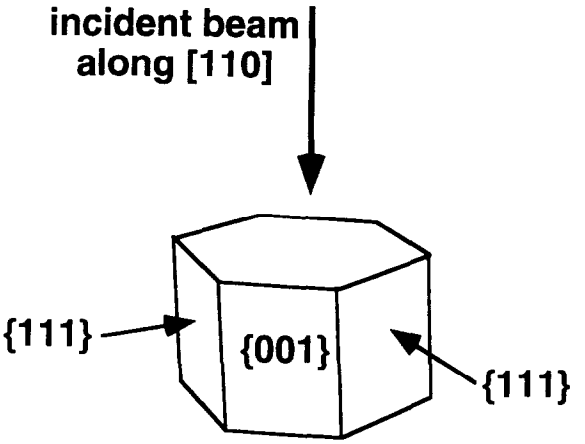

Figure 2. Schematic of the particle geometry suggested by the phase profile data. A right prism rather than a cuboctahedron better fits the observed phase profiles.

junction of the edge-on {111} facets at the point X would show a continuous, linear increase in thickness. The actual phase profiles instead show an abrupt phase change at the edge both for this direction as well as for most others (see, for example, the point labeled Y). In general, the profiles are also relatively flat across the particle interior. This suggests a prismatic morphology with all six apparent facets representing real bounding surfaces parallel to the beam, and approximately equal thickness along the beam direction in the central portion of the particle. A sketch of this possible morphology is shown in Figure 2. It should be noted that several other such particles were analyzed which showed clear correlation to the expected cuboctahedral morphology, rather than the prismatic morphology illustrated here. It is also important to recognize that even if the phase profile is representative of thickness, which requires the absence of electrical fields, magnetic fields, and dynamical scattering effects, it still does not provide an unambiguous shape because a variety of orientations of surfaces with respect to the beam are possible which could give the same phase image. However, other models require higher surface areas or re-entrant angles and are less likely to be energetically favorable (see (8) for details).

Model Combustion Catalysts: Pd on SiO_2

The active phase in heterogeneous catalysts consists of nanometer-sized metal or oxide particles dispersed within the tortuous pore structure of a high surface area matrix. Such catalysts are extensively used for controlling emissions from automobile exhaust or in industrial processes such as the refining of crude oil to produce gasoline. The morphology of these nanoparticles is of great interest to catalytic chemists since it affects the activity and selectivity for a class of reactions known as structure-sensitive reactions. In order to more effectively study particle morphologies and their changes during processing and use treatments, model specimens were chosen having supports of simple geometry on which metal particles were deposited.

The example specimens used here consisted of Pd particles supported on amorphous silica microspheres (9). Figure 3(a) shows a bright field HRTEM image of one of the Pd particles obtained after H_2 reduction of the calcined catalyst. We can see that the exposed face parallel to

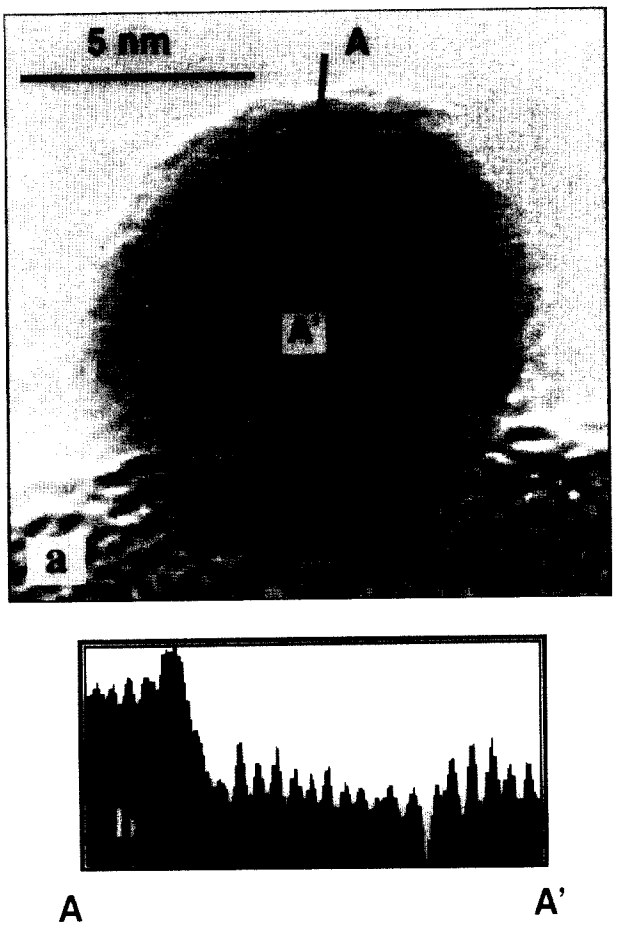

Figure 3. (a) High resolution TEM image of a Pd nanoparticle showing lattice fringes, indicating the particle is a single crystal; (b) intensity profile A-A' shows primarily fringe intensities and has no relation to particle morphology.

the electron beam direction is a (111) surface with a certain degree of surface roughness, which may arise in part from electron beam damage caused by observation of the particle at 1000 kX direct magnification. These particles have been shown by holography to contain internal voids, seen in this figure as the faceted central contrast feature (10). The lattice fringes are unaffected by the presence of the internal void and show that the Pd particle is a single crystal with no lattice defects. To illustrate that the HRTEM image does not directly provide information on the 3-dimensional shape of the metal particles, we have plotted in Figure 3(b) a histogram of image intensity along the line marked A-A' in Figure 3(a). This histogram does show the periodicity in contrast caused by the lattice fringes, but because of the nature of the image the 3-dimensional information is not retrievable.

Figure 4(a) shows the phase image derived from the hologram of this particle. Holoworks allows the choice of an appropriate aperture for the Fourier transformations, to de-emphasize the

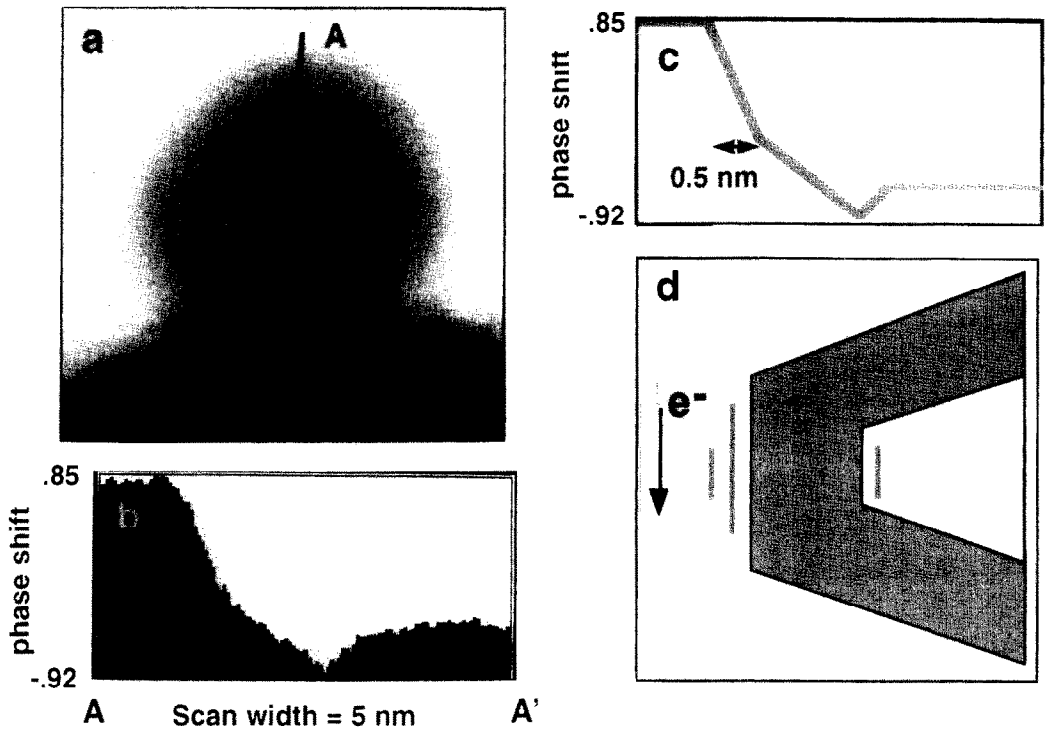

Figure 4. (a) Phase image reconstructed from hologram of particle of Figure 3; (b) phase profile along line A-A' of Figure 3; (c) schematic of phase profile which is consistent with the particle shape shown in (d). See text for details.

lattice fringe contrast in favor of the morphological details of the particle. Figure 4(b) shows a phase profile derived from the phase image along the line marked A-A' in Figure 3(a). It is seen that the phase shift is relatively flat in the vacuum surrounding the metal particle. The value of the phase shift has been arbitrarily set to 0.85. The phase shift changes rapidly with distance as the surface of the particle is encountered. These phase shifts are shown more clearly in Figure 4(c) with a cross-section model of the metal particle being shown in Figure 4(d).

Crystallography of Giant Nested Fullerenes

Polyhedral nested-shell carbon nanoparticles, or giant nested fullerenes, are often found as a byproduct of the carbon-arc discharge conditions that create carbon nanotubes (11). These particles can often be filled with the compounds of elements such as Gd or La, if oxides of these elements are incorporated appropriately into the arc discharge process (12). A typical giant nested fullerene structure encapsulating a Gd compound is shown in Figure 5. With these particles questions arose regarding the nature of the graphitized carbon structure. Graphite structures can range in the bulk from pure crystalline graphite to the fully turbostratic graphite structure where succeeding planes are randomly oriented (13-16). Turbostratic graphite shows no higher order

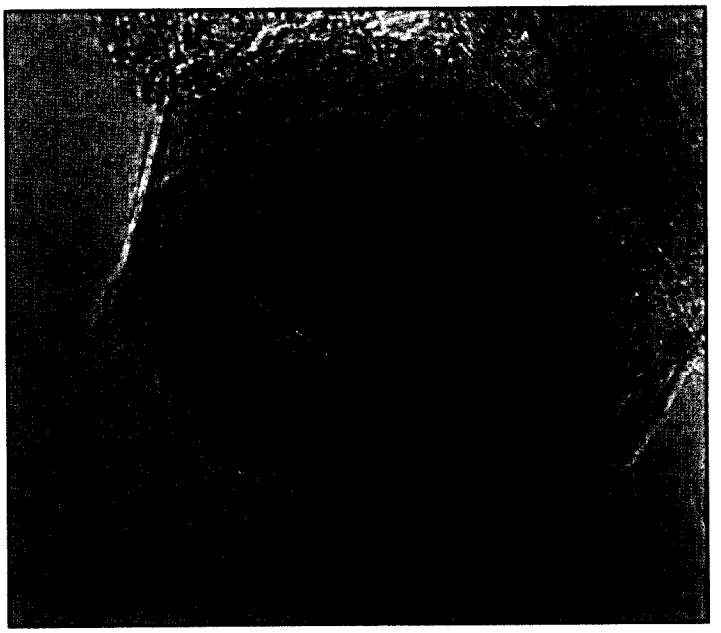

Figure 5. Giant nested fullerene encapsulating a gadolinium carbide particle.

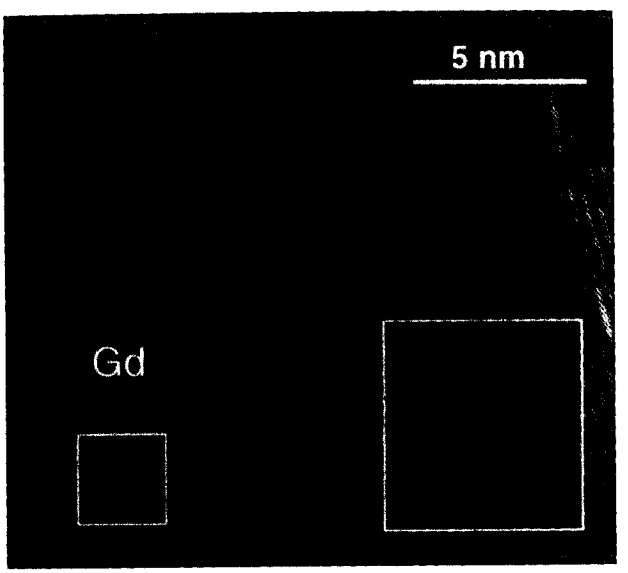

Figure 6. Electron hologram of a section of another particle showing graphite basal plane fringes in 256 x 256 pixel area (large outlined box) along with additional lattice fringes (running nearly horizontally). See text for details.

reflections in x-ray diffraction patterns, because there is order in only one direction—along the c-axis. The structure is said to be fully turbostratic when higher order peaks in the x-ray pattern disappear, at which point the basal spacing is typically 0.344 nm or greater (13-16). Bulk graphite which shows strong higher order reflections typically exhibits a basal plane spacing of 0.333 nm, the hexagonal graphite lattice spacing. Without a very accurate calibration of the magnification for an individual image in the TEM, no precise measurement can be made of the basal plane spacings in a given nanocrystal of a graphite-based material, such as partially graphitized carbon or a giant nested fullerene. Electron holography provides a means to determine lattice spacings with precision, as illustrated in the following example.

Figure 6 shows a hologram of a segment of a giant nested fullerene encapsulating a single crystal of a Gd compound (expected to be GdC_2 (11)). The hologram was recorded at 140 V on the biprism and at an instrument magnification of 1MX, with the specimen height adjusted to obtain the OL current required for optimum imaging. A 256^2 FFT of the area outlined is shown in Figure 7(a). In addition to the clear basal plane spacings within this area, a second set of apparent lattice spacings is evident. The reflections associated with both sets of planes are indicated on the FFT. In order to determine these spacings with precision, the distance of the sideband from the center of the autocorrelation was determined using a known crystal structure, in this case Si in the <110> orientation (Figure 7(b)). Care was taken to reproduce the operating conditions obtained for the fullerene hologram. The spacing of the hologram fringes at 140 V was calibrated using the "PEAK" measuring function provided by Holoworks. With this function, the distance of the center of a sideband was determined in pixels, with an accuracy of better than 0.05 pixels, using methodology developed by de Ruijter, *et al.* (17). With accurate calibration of the hologram, the

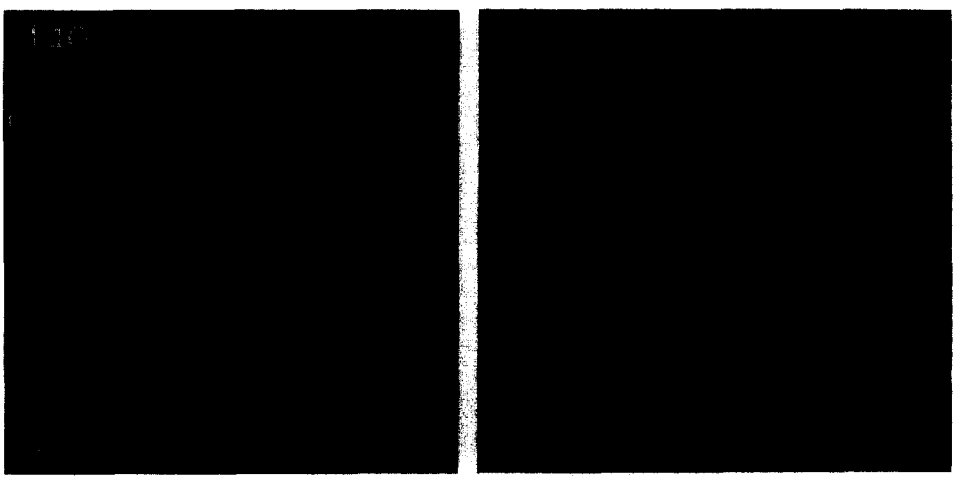

Figure 7. (a) FFT of 2562 area of Figure 6, showing (002) basal reflections and (101) reflections from additional lattice planes seen in Figure 6. The spacing of the basal planes was determined to be 0.353 nm, based on a precise calibration of the hologram fringes using a hologram recorded at the same fringe spacing (140 V on the biprism) from a single crystal silicon accurately oriented to a <110> zone axis as shown in (b). See text for details.

basal spacings observed in the fullerene particle were thus found to be 0.353 nm and the additional spacings were 0.206 nm. These latter spacings are consistent with the {101} reflections of pure graphite, and are properly positioned, as also determined by the PEAK program. The basal spacings are, however, significantly larger than the 0.335 nm expected for a pure hexagonal graphite structure and in fact are consistent with spacings found in purely turbostratic structures (*i.e.* d > 0.344 nm), where higher order reflections are not expected because of the random arrangement of each succeeding basal plane.

The reason for the development of the 0.353 nm basal plane separation is purely geometric. If the supergiant fullerene is considered to comprise a series of nested polyhedra, it results that an odd number of extra hexagons is added at each facet for each neighbor polyhedron, resulting in an ABABAB... stacking of polyhedral basal planes (see (18) for a detailed discussion). The nested polyhedra evidently are conformal (that is, they are similar geometric objects). Reduction of 0.353 (the experimental value) to 0.335 (the value for single crystal graphite) would mean a reduction in the c-c bond length of 5%, from a likely value of 0.1415 nm (the value appropriate for a graphene sheet) to that of 0.1342 nm. This is much too costly in energy, so the covalent bonding network (and the conformal layering) determines the interlayer separation. It is interesting to note that this 0.353 nm interlayer spacing has been observed in BN films deposited onto MgO nano-cubes (smoke particles) (19). Since BN is a structural analogue to graphite, these films on MgO mimic the morphologies observed in the encapsulation of carbides by graphite which form giant nested fullerene structures. The presence of lattice planes consistent with higher order reflections in high resolution images of the BN on the MgO cubes, even though the basal plane spacing was clearly consistent with a fully turbostratic structure, suggests that the structures observed in giant nested fullerenes are not anomalies.

The calibration of the hologram spacings permits also the measurement of lattice spacings associated with the Gd crystal being encapsulated. Although not easily visible in the digital image of Figure 8, the FFT from the 128^2 region outlined on the Gd area showed faint reflections, indicating the presence of lattice planes in the image having a spacing of 0.161 nm. This corresponds to the {210} reflections of GdC_2, a result consistent with x-ray observations from bulk materials.

CONCLUSIONS

Among many applications of electron holography which are being developed, its potential for providing precise information about the shapes of nanoparticulates is of interest in the fields of nanostructured materials such as nanophase ceramics, fullerene materials and catalysts. We have demonstrated here that combining the analysis of pure phase images, reconstructed from holograms of nanoparticles, with *a posteriori* knowledge about the particle obtained from the high resolution images, allows much information about particle shapes to be determined that can be obtained with no other method. The additional facility for analysis of crystallographic aspects of the materials with high precision is a bonus provided by electron holography.

ACKNOWLEDGMENTS

Research sponsored by the Laboratory Directed Research and Development Program of Oak Ridge National Laboratory, and by an appointment (A.K.D.) to the High Temperature Materials

Laboratory Faculty Fellowship Program, sponsored by the Assistant Secretary for Energy Efficiency and Renewable Energy, Office of Transportation Technologies, under contract DE-AC05-84OR21400 with Martin Marietta Energy Systems, Inc.

REFERENCES

1. D.J. Smith, MH. Yao, L.F. Allard and A.K. Datye, Catal. Lett. 31, 57 (1995).
2. H. Lichte, Adv. in Optical and Electron Microscopy 12, 25 (1991).
3. A. Tonomura, *Electron Holography*, Springer-Verlag (1993).
4. G. Möllenstedt and H. Düker, Z. Physik 145, 377 (1956).
5. E. Voelkl, B. Frost and L. F. Allard, *Proceedings 1st International Workshop on Electron Holography*, Elsevier (1995), in press.
6. M. Gajdardziska-Josifovska, M.R. McCartney, W.J. de Ruijter, D.J. Smith, J.K. Weiss, and J.M. Zuo, Ultramicroscopy 50, 285 (1993).
7. M. ÇiftÇioglu and M.J. Mayo, in *Superplasticity in Metals, Ceramics, and Intermetallics*, eds. M.J. Mayo *et al.*, Mat. Res. Soc. Symp. Proc. 196, 77 (1990).
8. A.H. Carim, L.F. Allard, E. Voelkl and B.G. Frost, submitted to J. Mater. Research (1995).
9. W. Stoeber, A. Fink and E. Bohn, J. Colloid Interface Sci. 26, 62 (1968).
10. L.F. Allard, E. Völkl, D. Kalakkad and A.K. Datye, J. Mat. Sci. 29, 5612 (1994).
11. S. Iijima, Nature 354, 56 (1992).
12. R.S. Ruoff, D. Lorents, B. Chan, R. Malhotra, and S. Subramoney, Science 259, 346 (1993).
13. W. Ruland, Acta Cryst. 18, 992 (1965.
14. D.B. Fishbach, *Chemistry and Physics of Carbon*, Vol. 7, ed. P.L. Walker, Marcel Dekker , p. 7 (1968).
15. M. Shioya and A. Takaku, Carbon 28(1), 165 (1990).
16. J. Biscoe and B.E. Warren, J. Appl. Phys. 13, 364 (1942).
17. W.J. deRuijter *et al.*, Scanning Microsc. Supp. 6, 347 (1992).
18. D.C. Lorents, R.S. Ruoff, R. Malhotra and S. Subramoney, Mol. Mat. 4, 15 (1994).